Highlights

Beam-hardening corrections through a polychromatic projection model integrated to an iterative reconstruction algorithm

Leonardo Di Schiavi Trotta,Dmitri Matenine,Margherita Martini,Karl Stierstorfer,Yannick Lemaréchal,Pier
Francus,Philippe Després

- Polychromatic projection model reduces beam-hardening artifacts in X-ray CT.
- Image artifacts are reduced using CT scanner information: filter and X-ray spectrum.
- Numerically intense CT reconstructions with X-ray spectrum are accelerated by GPUs.

Beam-hardening corrections through a polychromatic projection model integrated to an iterative reconstruction algorithm

Leonardo Di Schiavi Trotta[a,1], Dmitri Matenine[c], Margherita Martini[b], Karl Stierstorfer[d], Yannick Lemaréchal[a], Pierre Francus[b] and Philippe Després[a,*]

[a] *Department of Physics, Physical Engineering, and Optics, Université Laval, 1045, av. de la Médecine G1V 0A6, Québec, Québec, Canada*

[b] *Centre Eau Terre Environnement, Institut National de la Recherche Scientifique, 2605 Boulevard du Parc Technologique G1P 4S5, Québec, Québec, Canada*

[c] *Département de génie des systèmes, École de technologie supérieure,1100 Rue Notre-Dame Ouest H3C 1K3, Montréal, Québec, Canada*

[d] *Siemens Healthcare, Computed Tomography, 91301 Siemensstraße 1, Forchheim, Bavaria, Germany*

ARTICLE INFO

Keywords:
Beam-hardening correction
Iterative reconstruction
Computed Tomography
GPU acceleration
Dual-energy Computed Tomography

ABSTRACT

In this work, a novel physics-rich beam-hardening correction algorithm was developed for X-ray Computed Tomography. This method uses the spectrum information, the detector response, the filter geometry and a calibration curve. The correction, which does not require prior material knowledge, was embedded in an iterative reconstruction algorithm, and simulates the beam-hardening by estimating the X-ray spectrum at each voxel in the forward projection step. As a result, beam-hardening artifacts are inherently reduced in reconstructed images. For a regular reconstruction matrix of 512 pixels x 512 pixels, processing times of approximately ∼5 s per slice were obtained using a four GPU setup. This method was also compared to the dual-energy beam-hardening correction method proposed by Alvarez and Macovski, which it outperforms when high-Z elements are involved.

*Corresponding author

leonardo.di-schiavi-trotta.1@ulaval.ca (L.D.S. Trotta); dmitri.Matenine@etsmtl.ca (D. Matenine); Margherita.Martini@inrs.ca (M. Martini); karl.stierstorfer@siemens-healthineers.com (K. Stierstorfer); yannick.lemarechal.1@ulaval.ca (Y. Lemaréchal); pierre.francus@inrs.ca (P. Francus); philippe.despres@phy.ulaval.ca (P. Després)

ORCID(s): 0000-0001-8739-5655 (L.D.S. Trotta); 0000-0002-9663-4459 (D. Matenine); 0000-0002-5227-2804 (M. Martini); 0000-0002-4304-9731 (K. Stierstorfer); 0000-0002-2494-2831 (Y. Lemaréchal); 0000-0001-5465-1966 (P. Francus); 0000-0002-4163-7353 (P. Després)

[1] Currently PhD student at Université Laval.

1. Introduction

X-ray Computed Tomography (CT) is now ubiquitous in medicine for diagnostic and follow-up purposes. This technology is also increasingly used for non-medical purposes in several fields, notably for high-resolution, non-destructive analysis [1].

The presence of high-density materials in scanned objects causes deterioration of CT image quality; the polychromatic nature of the X-ray beam used in CT scanners is at the origin of some image artifacts (e.g. streaks and cupping artifacts) [2]. Physical and non-physical models for beam hardening correction (BHC) were proposed to tackle this problem. This includes: the use of physical filters to pre-harden the beam, X-ray absorption considerations in the iterative reconstruction (IR) algorithm [3], effective energy shift of the X-ray spectrum in each voxel in the forward projector step of the IR algorithm [4] and dual-energy (DE) methods which inherently corrects for such artifacts [5, 6, 7, 8]. This latter method is known for producing images with amplified noise [6] in the CT energy range due to the nature of the photoelectric effect. Most methods require the knowledge of the material composition, which is not ideal for non-medical applications, since characterization is often the main objective. The heterogeneity of most samples requires physics-rich algorithms, capable of modelling the X-ray attenuation in the image formation process, without having to rely on prior material information.

The Multidisciplinary Laboratory of CT-Scan for Natural Resources and Civil Engineering, located at INRS Eau Terre Environnement in Quebec City, is the first Canadian facility equipped with a CT scanner adapted for non-medical use. This modified CT scanner, mounted on rails, is able to acquire data of long samples, including from experiments in a custom-made hydraulic channel, for research activities in Earth and Environmental Sciences (*e.g.* sedimentology, forestry, geology, oceanography). This equipment can be used to scan diverse samples including drilling cores from land, oceans or lakes. The CT provides 3D images that relate to their structural organization and density distribution [9].

In a clinical environment, filtered back-projection algorithms such as the one described by Feldkamp, Davis, and Kress [10] are often used. Advances in computing power have driven the development of iterative reconstruction algorithms (IR), which allow acquisitions with reduced dose, noise and number of projections [11]. This class of reconstruction algorithms are numerically intensive, typically requiring GPU computing to get results in reasonable time [12]. In principle, the inclusion of physics phenomena pertaining to the image formation process into the reconstruction algorithm would lead to images of higher quality. Artifacts such as beam hardening can potentially be reduced by integrating more physics in the reconstruction process, for example by simulating the polychromatic behavior of the X-ray beam in the forward projector step [4].

We have developed a polychromatic projection model that uses the spectrum information, the detector response, the filter geometry of the CT scanner and a calibration curve to properly model the physics in the IR algorithm. As opposed to other approaches [3, 13], this algorithm requires no prior knowledge of the material composition, material assumption or material segmentation [14]. The numerical burden associated with such advanced modeling is offloaded by the use of multiple GPUs. With this approach, we aim at inherently reduce beam-hardening artifacts in reconstructed images through a polychromatic forward projection model, whereas standard reconstruction typically assumes a monochromatic X-ray beam. We compared this approach to a dual-energy beam-hardening correction method based on the work of Alvarez and Macovski (DE-AM) [5, 8].

This paper is divided as follows: in Section 2, the polychromatic projection model is introduced, as well as the equations used to perform the dual-energy beam-hardening correction. Both models require the spectral response of the detector, which is presented at the end of this section. In Section 2.2, the integration of spectral information in the forward projection model is described for the iterative algorithm OSC-TV, a combination of Ordered Subsets Convex (OSC) algorithm and the Total Variation minimization (TV) regularization technique [11, 15]. Section 2.5 reports simulation work conducted prior to real-world experiments as well as details regarding the acquisition and reconstruction parameters. Finally, Section 3 reports the results including the calibration curve required by the proposed approach and the comparison with the dual-energy beam-hardening correction.

2. Materials and Methods

2.1. Polychromatic forward projection

For a polychromatic beam traversing a heterogeneous material, the projection value P_i in the sinogram is given by the following expression [16]:

$$P_i = -\ln\left\{\frac{\int s(E)d(E)\exp\left\{-\int_L \mu(E,r)dr\right\}dE}{\int s(E)d(E)dE}\right\}, \tag{1}$$

where $s(E)$ is the X-ray spectrum of the source, $d(E)$ is the energy-dependent detector response, $\mu(E,r)$ the linear attenuation coefficient at position r along the path L evaluated at the energy E of the X-ray spectrum. In the forward projector step of most IR algorithms, a much simpler model is generally used, where the total attenuation is calculated as follows:

$$P_i = \sum_{j\in i} l_{ij}\mu_j, \tag{2}$$

where μ_j is the linear attenuation coefficient in voxel j, traversed by the ray i, and l_{ij} is the intersection length.

We posit that the total attenuation can be transformed from monochromatic to polychromatic by introducing the attenuation coefficient averaged over the local spectral response, also called local attenuation coefficient [17]:

$$\mu_{s_j} = \frac{\sum_{k=0}^{K} s'_{jk}\mu_{jk}}{\sum_{k=0}^{K} s'_{jk}}, \tag{3}$$

where k is the energy index, K the total number of energies, μ_{jk} the linear attenuation coefficient in voxel j at energy k, and s'_{jk} is the spectral response ($s'_{jk} = d_k \cdot s_{jk}$) in voxel j at energy k, in which s_{jk} is the correspondent X-ray spectrum and d_k is the detector response. The local spectral response in j is attenuated by $j-1$ voxels, and is calculated by the following expression:

$$s'_{jk} = s'_{0k} \exp\left\{ -\sum_{j' \in i}^{j-1} l_{ij'} \mu_{j'k} \right\}, \tag{4}$$

where s'_{0k} is the unattenuated spectral response at energy k. Thus, a polychromatic projection have the following form:

$$P_i = \sum_{j \in i} l_{ij} \mu_{s_j}. \tag{5}$$

For simplification purposes, the linear attenuation coefficient at energy E_k can be decomposed into photoelectric and Compton contributions [5, 18]:

$$\mu_k = a_p E_k^{-3} + a_c f_{KN}(E_k), \tag{6}$$

where a_p and a_c are constants related to each physical process, f_{KN} is the Klein-Nishina function and E_k corresponds to the energies of the discretized spectrum. If we suppose that the uncorrected linear attenuation coefficient μ_j is evaluated at the effective energy of the X-ray spectral response

$$E_0 = \frac{\sum_{k=0}^{K} s'_{k0} E_k}{\sum_{k=0}^{K} s'_{k0}}, \tag{7}$$

we can estimate the attenuation in voxel j at any energy k using the following relation:

$$\mu_{jk} \approx \frac{\left(\frac{a_p}{a_c}\right)_j E_k^{-3} + f_{KN}(E_k)}{\left(\frac{a_p}{a_c}\right)_j E_0^{-3} + f_{KN}(E_0)} \mu_j = f_{jk} \cdot \mu_j. \tag{8}$$

where f_{jk} is the conversion factor, which estimates the attenuation coefficient at any energy E_k of the X-ray spectrum for the voxel j as a function of the uncorrected attenuation mu_j. If the spectral response is known, the only quantity yet to be determined is the ratio $(a_p/a_c)_j$, which gives the contribution of each physical effect in each voxel. This quantity can be estimated through a calibration curve of the form:

$$\left(\frac{a_p}{a_c}\right)_j = \sum_m b_m \mu_{E_0}^m \approx \sum_m b_m \mu_j^m, \tag{9}$$

where μ_{E_0} is the linear attenuation coefficient evaluated at E_0, which is roughly equal to the uncorrected μ_j in our approximation. The curve is calibrated against μ_{E_0}. However, during the forward-projection step of the reconstruction, $(a_p/a_c)_j$ is determined by applying μ_j in Eq. 9.

2.2. Incorporating the forward projection in OSC-TV

Reconstruction algorithms are based on the Beer-Lambert law and therefore assume a monoenergetic photon beam. Photon counts Y_i, for a detector element i, are Poisson-distributed as:

$$Y_i = b_i e^{-t_i} \tag{10}$$

where b_i is the incident photons count and $t_i = \sum l_{ij} \mu_j$.

In the context of energy-integrating detectors (EIDs), b_i will represent the energy read by such a detector. In this case, the measured quantity Y_i will not strictly follow a Poisson distribution, however, such model can still be considered a good approximation [3].

The data correspondence step maximizes the Poisson log-likelihood $L(\mu)$ of the image estimate μ and is written as follows:

$$L(\mu) = -\sum_{i} \left(b_i e^{-t_i} + Y_i t_i \right), \tag{11}$$

where the maximum of this function with respect to μ is the best fit of the image estimate to projection data Y. The OSC algorithm is used to accelerate the convergence rate [19]. In this algorithm, a few projections in sequence are used to project and back-project the estimated image in order to update μ:

$$\mu_{s+1}^{(n)} = \mu_s^{(n)} + \mu_s^{(n)} \frac{\sum_{i \in S(s)} l_{ij} \left[\bar{y}_i^{(n)} - Y_i \right]}{\sum_{i \in S(s)} l_{ij} t_i^{(n)} \bar{y}_i^{(n)}}, \tag{12}$$

in which n is the reconstruction iteration number, $\bar{y}_i = b_i e^{-t_i^{(n)}}$ is the estimated photon count or energy imparted in the detector, s is the index of the subset and $S(s)$ is the function which generates the subsets of rays associated with the projections that are selected for the iteration. As an input for the iterative reconstruction, one defines the initial and final number of subsets. An initial high number of subsets increases the convergence rate of the reconstruction. This number of subsets is reduced at each iteration in order to reduce the bias in reconstruction [20, 21]. At the end of a full OSC iteration step, the resulting image is regularized by the total variation minimization technique (TV), which decreases the noise [11].

In order to implement a polychromatic model in OSC-TV, and following Eq. 5, we substituted the total attenuation $t_i^{(n)}$ in Eq. 12 and in the parameter $\bar{y}_i^{(n)}$ by:

$$t_i^{(n)} = \sum_{j \in i} l_{ij} \mu_{s_j}^{(n)}, \tag{13}$$

where l_{ij} and μ_{s_j} are evaluated at each voxel in the forward projections step. The total attenuation t_i is calculated using the Siddon raytracing algorithm [22]. This algorithm allows us to keep track of the X-ray spectrum at each voxel using the equations defined in section 2.1, as this quantity is calculated through a loop over each voxel traversed by the ray i. With that, we determine each term of Eq. 13.

The strategy used to implement the polychromatic projection model is summarized in Fig. 1. For the sake of simplicity, we consider that s_{jk} is the detector spectral response and that $\mu_j^{(n)} = \mu_j$. Within the forward projection step of an IR algorithm, and for each energy E_k of the X-ray spectrum, given an arbitrary voxel j, where $j \in i$, the estimated and uncorrected attenuation μ_j is used first to calculate the Compton and photoelectric coefficients by using the calibration curve given by Eq. 9. Once these terms are defined, one can obtain the conversion factor f_{jk}, which can be used to estimate μ_{jk} (see Eq. 8). The total attenuation for the energy E_k, henceforth defined as T, is then accumulated over $j-1$ voxels and used to calculate the spectrum response for each energy bin at the voxel j. Once all energy bins are processed, the local attenuation coefficient can be calculated by applying Eq. 3, leading to the total attenuation given by Eq. 13.

2.3. Dual-energy decomposition

Following the DE-AM method [5, 6, 8, 7], with two scans acquired with different tube voltages, one obtains two sets of logarithmic projections, P_L and P_H. In order to calculate $A_p = \sum a_p l_{ij}$ and $A_c = \sum a_c l_{ij}$, the photoelectric absorption and Compton scattering line integrals, the multivariate Newton-Raphson method was used to minimize the following system of equations [6, 7]:

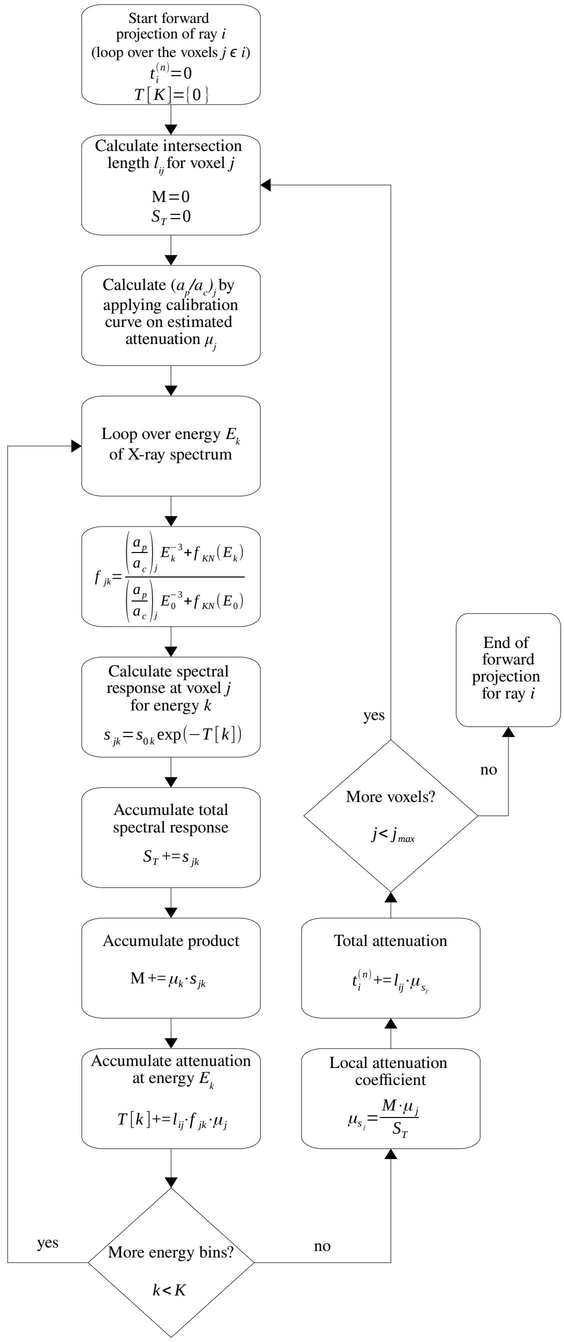

Figure 1: Flowchart depicting the strategy used to implement the polychromatic forward projection in the OSC-TV algorithm.

$$f_L = -\ln \sum_k s_{Lk} d_k \exp\left[-A_p E_k^{-3} - A_c f_{KN}(E_k)\right] + \\ + \ln \sum_k s_{Lk} d_k - P_L, \quad (14)$$

$$f_H = -\ln \sum_k s_{Hk} d_k \exp\left[-A_p E_k^{-3} + A_c f_{KN}(E_k)\right] + \\ + \ln \sum_k s_{Hk} d_k - P_H, \quad (15)$$

where s_{Lk} and s_{Hk} are the low- and high-energy X-ray spectrum. The pair (A_p, A_c) is updated as follows:

$$\begin{pmatrix} A_p^{[n+1]} \\ A_c^{[n+1]} \end{pmatrix} = \begin{pmatrix} A_p^{[n]} \\ A_c^{[n]} \end{pmatrix} - \left[J^{-1}_{(f_L, f_H)}(A_p^{[n]}, A_c^{[n]})\right] \begin{pmatrix} f_L(A_p^{[n]}, A_c^{[n]}) \\ f_H(A_p^{[n]}, A_c^{[n]}) \end{pmatrix}, \quad (16)$$

where J^{-1} is the inverse of the Jacobian of the functions f_L and f_H evaluated at $A_p = A_p^{[n]}$ and $A_c = A_c^{[n]}$. The iteration stops when $|A_p^{[n+1]} - A_p^{[n]}| < 10^{-6}$ and $|A_c^{[n+1]} - A_c^{[n]}| < 10^{-6}$.

The minimization is accelerated by the use of an nVidia graphic card RTX 2070 SUPER, using the Numba compiler [23]. With this module, a portion of the python code can be compiled into CUDA kernels and device functions, allowing GPU parallel computation with a fast implementation.

The solution obtained is not always a physical one, mainly when noise is present in the projection data. It means that either A_p or A_c is negative or undefined. Therefore, a constrained decomposition method was used [6, 7], with minor modifications to deal with undefined solutions.

With the line integrals, A_p and A_c, calculated from P_L and P_H, the iterative algorithm OSC-TV (Section 2.2) [11, 15] was used to reconstruct the photoelectric and Compton images, a_p and a_c, respectively. This algorithm runs on multiple GPUs, which delivers a computation time ranging from seconds to minutes depending on the number of projections and the detector grid size. From these images, the virtual monoenergetic image (VMI) evaluated at energy E_k is obtained by applying Eq. 6.

2.4. Detector dependent spectrum

Medical CT scanners are equipped with bowtie filters, generally made of aluminum. Those filters are used to compensate the differential hardening of the beam as it passes through the scanned sample. Such assembly is responsible for reducing cupping artifacts in medical applications [24].

The methods detailed in Sections 2.1 and 2.3 for BHC require the prior knowledge of the X-ray spectrum. Given that the spectrum is typically "pre-hardened" by the bowtie filter in medical CT scanners, one must take into account such effect. By modelling the bowtie filter, one can calculate the spectrum as a function of the CT fan angle θ, and incorporate the detector dependent spectrum into the previous models through the following equation:

$$s_k(\theta) = s_k \exp\left[-x(\theta)\mu_{Al}(E_k)\right], \tag{17}$$

where x is the thickness of aluminum traversed by the beam and μ_{Al} is the linear attenuation coefficient for aluminum. The spectra and the detector response used in this work, both necessary for applying our BHC method and the DE-AM method, are the ones provided by the manufacturer.

2.5. Imaging process

The scans were performed using a Siemens SOMATOM Definition AS+ 128 CT scanner, installed at INRS Eau Terre Environnement in Quebec City. In this work, we used vendor-provided binaries to remove the proprietary beam-hardening correction (BHC) preprocessing and to convert raw data into convenient image file format. All samples were scanned in sequential mode.

2.5.1. Numerical simulations

In order to validate the proposed method, simulations of sequential acquisitions were conducted for 100 kVp and 140 kVp with a virtual phantom, taking into account the geometry of the Siemens SOMATOM Definition AS+ 128 CT scanner as well as the same X-ray spectra and detector response provided by the manufacturer. For simplification purposes, the bowtie filter was not con-

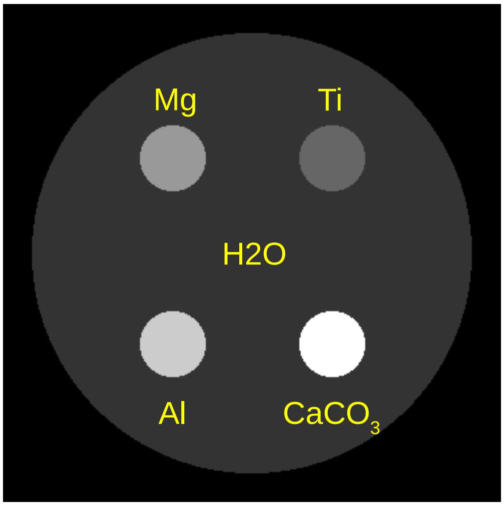

Figure 2: Virtual phantom.

sidered for this case nor any noise model, hence, no dependence of the X-ray spectra on the CT fan angle. A sequential acquisition protocol was simulated, where 2,304 projections are acquired over a single rotation through the use of a flying focal spot. A detector grid of dimensions 736 pixels x 64 pixels was used. The virtual phantom, illustrated in Fig. 2, is composed of a water cylinder of 200 mm of diameter, with 4 cylinder rods of 30 mm of diameter. The material properties of the virtual phantom are reported in Table 1.

Table 1
Composition of the virtual phantom.

material	Z_{eff}	ρ_e $(\frac{electrons \cdot mol}{cm^3})$	ρ $(\frac{g}{cm^3})$
Water (H_2O)	7.42	0.555	1.000
Titanium (Ti)	22	2.071	4.506
Magnesium (Mg)	12	0.858	1.738
Aluminum (Al)	13	1.301	2.700
Marble ($CaCO_3$)	15.08	1.354	2.711

The effective atomic number Z_{eff} was obtained through the classical expression [25]:

$$Z_{eff} = \sum_i \sqrt[\beta]{\lambda_i Z_i^{\beta}}, \tag{18}$$

where β is usually a value defined between 2.94 and 3.80, which is usually judiciously obtained depending on a set of materials for characterization purposes [7, 26]. Finally, λ_i is the fraction number of electrons, which is given by:

$$\lambda_i = \frac{n_i Z_i}{\sum_{j=1}^{N} n_j Z_j}, \tag{19}$$

where n_i represents the number of atoms of the composition having an atomic number Z_i.

The electron density ρ_e for a compound may be calculated by the giving formulas [27]:

$$\rho_e = \rho N_A \left(\frac{Z}{A}\right)_{med}, \tag{20}$$

$$\left(\frac{Z}{A}\right)_{med} = \sum_i \omega_i \left(\frac{Z_i}{A_i}\right), \tag{21}$$

where ω_i the fractional weight of the chemical element i in the compound, N_A is the Avogadro's number, ρ is the mass density, A_i is the atomic weight of the element i, and the ratio $(Z/A)_{med}$ is the ratio of the atomic number to the atomic weight of a given medium.

2.5.2. Real-samples application

Three samples were used to illustrate the performance of both algorithms in a real scenario (see Fig. 3): (i) a water phantom with a diameter of 200 mm; (ii) an aluminum cylinder with a diameter of 75 mm, corresponding to the leftmost part of Fig. 3 (b); (iii) a sodium iodide solution (NaI) with at 50 % concentration in a 13.5 mm diameter recipient. This solution presents an effective atomic number of 37.53 and an electron density of $\rho_e = 0.671\ e^- \cdot mol/cm^3$.

For the water phantom and the aluminum sample, the same scanning protocol was used, where

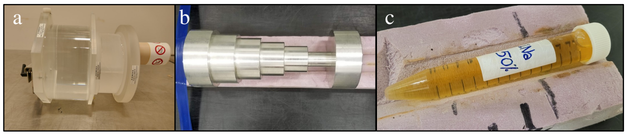

Figure 3: Samples used to test our beam-hardening correction algorithm: (a) Water phantom for Definition AS, (b) aluminum sample and (c) 50 % NaI solution.

2,304 projections are generated by two distinct flying focal spots over a single rotation, with a detector grid with dimensions 736 pixels x 64 pixels. Due to the small size of the 50 % NaI solution, a protocol that generates 4,608 projections through four flying focal spots was used instead, with the same detector grid size. The respective bowtie filter set in such scanning mode was properly modelled as to account for the spectrum as function of the fan angle (Section 2.4).

In order to appreciate the effect of the bowtie filter modelling for beam-hardening correction, its effect was also removed for the water phantom. Hence, two different scenarios can be shown: BHC with and without bowtie filter modelling. For the last case, the X-ray spectra used in the corrections are not "pre-hardened" by the filter, while for the first case it depends on the CT fan angle, as given in Eq. 17. For the other samples, such as the aluminum and the 50 % NaI solution, the effect of the bowtie filter on the X-ray spectra was included in the BHC approaches.

Each sample was scanned with a tube voltage of 100 kVp and 140 kVp, so that the dual-energy method (DE-AM) can be applied. For the water phantom, a tube current of 420 mA was used, with a corresponding value of 600 mA for the aluminium sample, in both cases with an exposition time of 0.5 s. Finally, the 50 % NaI solution was scanned with a tube current of 550 mA for the 140 kVp and 600 mA for the 100 kVp tube voltage, and 1.0 s of exposition time.

The OSC-TV was used both with and without the polychromatic projection model, henceforth called OSC-TV-poly (Section 2.1), to reconstruct the images of the virtual phantom and the real samples acquired at an X-ray tube voltage of 140 kVp. For the dual-energy method, the 100 and 140 kVp projections were transformed into photoelectric and Compton components (see Eqs. 14 and 15), which are later reconstructed with the OSC-TV algorithm. Finally, these dual-energy images were combined (see Eq. 6) to produce a VMI at the effective energy E_0 of the 140 kVp

Table 2
Reconstruction matrix size and voxel size defined for the OSC-TV and the OSC-TV-poly algorithm. The same parameters are used for the 140 kVp, photoelectric and Compton images of each sample.

Samples	Matrix size	Voxel size (mm^3)
virtual phantom	512 x 512 x 24	0.6 x 0.6 x 1.2
water phantom	512 x 512 x 16	0.78 x 0.78 x 2.0
aluminum	512 x 512 x 48	0.6 x 0.6 x 0.6
50 % INa	2048 x 2048 x 48	0.15 x 0.15 x 0.6

beam.

2.5.3. Reconstruction parameters

Images are reconstructed in units of cm^{-1}, and not in Hounsfield units (HU). As the manufacturer beam-hardening preprocessing was removed from the raw data, the water pixel values are no longer normalized to 0 HU, and so they reflect the linear attenuation coefficient at the effective energy of the source's X-ray spectrum.

For each sample, different sets of reconstruction parameters for the OSC-TV algorithm were used (e.g. number of iterations, initial number of subsets, final number of subsets, voxel size, grid size), as well as regularization parameters related to TV minimization [11] (see Tables 2 and 3). All the reconstructions, including the 140 kVp, photoelectric and Compton images, were performed using the same number of iterations, a regular grid size of 512 pixels x 512 pixels, except for the 50 % NaI solution, where a grid size of 2048 pixels x 2048 pixels was used (see Table 2). The reconstruction matrix size in z depends on its respective voxel size. The voxel size in x and y was adjusted so that the scanned object and the CT scanner table are included in the field-of-view (FOV). This is necessary to avoid truncation artifacts related to objects outside the image grid [28].

As one can note in Table 3, a higher number of subsets (and a final number of subsets) was used for the virtual phantom. This configuration increases the convergence rate [20] and is necessary due to the high attenuating materials (e.g. titanium) present in such sample.

The regularization constant dictates the strength of the regularization performed by TV (e.g. smoothness). The same TV constant value was used for all 140 kVp images, to preserve spa-

Table 3
Reconstruction parameters for the OSC-TV and the OSC-TV-poly algorithm. The number of iterations, number of subsets and the final number of subsets are the same for the 140 kVp, photoelectric and Compton images of each sample.

Samples	OSC-TV/OSC-TV-poly parameters			Regularization constant		
	Number of iterations	Number of subsets	Final number of subsets	140 kVp	Photoelectric	Compton
Virtual phantom	5	800	80	0.02	0.02	0.02
Water phantom	5	84	9	0.02	0.4	0.1
Aluminum	5	84	9	0.02	0.4	0.1
50 % NaI	5	84	9	0.02	0.1	0.1

tial resolution. As summarized in Table 3, for real samples, the same reconstruction parameters were used. The correspondent photoelectric and Compton images of the water phantom and the aluminum sample are reconstructed with a larger regularization constant, while for the 50 % NaI solution, this constant was set to 0.1 for the Compton and photoelectric images. By doing this, the inherent noise of both projections are attenuated. It is worth noting that further research could better guide the choice of the regularization parameter and lead to optimal reconstructions in terms of noise and spatial resolution.

The OSC-TV-poly is computationally intensive. Hence, in order to evaluate the applicability of our method, reconstructions with both OSC-TV and OSC-TV-poly were performed on a computing node with four nVidia V100 Volta GPUs.

In order to evaluate potentially cupping and capping artifacts generated in the reconstructed images, a beam-hardening ratio is defined as [6]:

$$BHR = \frac{\left|P_{edge} - P_{center}\right|}{P_{edge}} \times 100\%, \tag{22}$$

in which P_{edge} and P_{center} are the pixel values at the edge and at the center of the reconstructed image, obtained from the line profiles illustrated in Figs. 6, 8 and 9.

3. Results and discussion

3.1. Calibration curve

Eq. 6 was used to fit, with the least square method and data from the NIST XCOM database [29], the linear attenuation coefficient of a large list of materials compiled by Barthelmy [30] (e.g. 3,000 materials and constrained by $Z_{eff} \leq 27$ and $\rho \leq 5.2g/cm^3$). Attenuation coefficient were considered in the 20 to 140 keV energy range to obtain the (a_p,a_c) pairs. Fits with coefficient of determination R^2 higher or equal to 0.999 were used. This constraint mainly removes elements that present K-edges within the energy range considered and that act as outliers in the fit procedure. Finally, the ratio a_p/a_c obtained for each material is fitted against its respective attenuation evaluated at the effective energy of the X-ray spectral response, $\mu(E_0 = 83\ keV)$, where E_0 is the effective energy of the 140 kVp beam. For that, a polynomial of order 6, with the constraint that the first parameter b_0 is always zero, was used. By those means, the ratio a_p/a_c is always greater than zero for low values of $\mu(E_0)$. For this fitting procedure, it was obtained an $R^2 = 0.893$ (Fig. 4).

One may define an adapted calibration curve by knowing *a priori* the nature of what is being scanned, hence, limiting its range for specific materials. This approach could improve the X-ray spectrum estimation through more accurate Compton and photoelectric contributions, further reducing beam-hardening artifacts. A similar approach was used by de Man *et al.* [3], where material assumptions is required. It is worth noting that the number of iterations for OSC-TV and OSC-TV-poly remains the same, hence, no extra forward-projections and back-projections are required in the model, and neither the reconstruction of extra images, as only the forward-projection step is changed.

3.2. Simulation results

Fig. 5 shows the comparison between the reconstruction of the virtual phantom with no BHC (a), the DE-AM method (b) and the proposed BHC method(c). As the X-ray spectra and the detector response are well known in the simulation framework, the dual-energy method efficiently removes beam-hardening artifacts, such as dark streaks and cupping. No bowtie filter modelling was used,

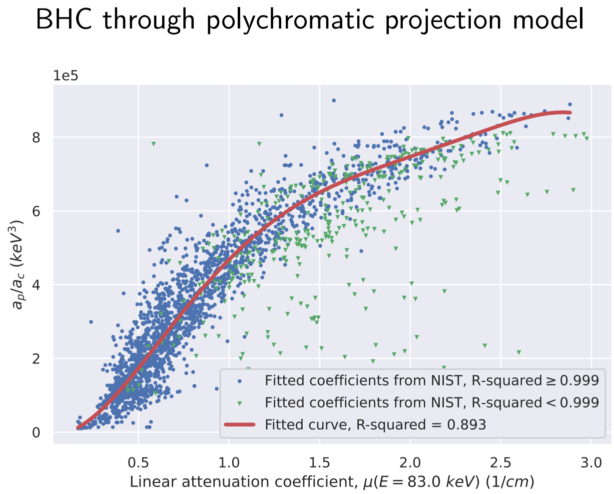

Figure 4: Calibration curve used to estimate a_p/a_c from the uncorrected linear attenuation coefficient.

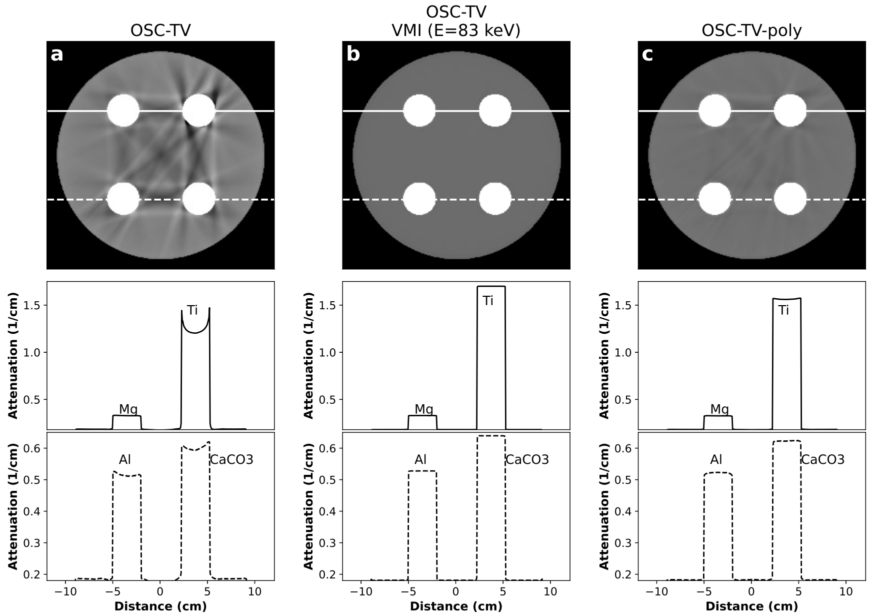

Figure 5: Virtual phantom: (a) reconstruction performed with OSC-TV (140 kVp), (b) virtual monoenergetic image calculated through DE-AM method (100/140 kVp), evaluated at 83 keV, (c) reconstruction performed with OSC-TV-poly (140 kVp). Window: [0.160, 0.200] cm^{-1}.

as it was not included in the virtual acquisition. Hence, the X-ray spectra are the same for all the detector elements of the CT scanner. The OSC-TV-poly method also produces images with reduced BH artifacts, for both water and other materials. These results suggest that the OSC-TV-poly algorithm can handle a wide range of Z_{eff} and ρ_e without having to rely on semi-empirical parameters which might not be optimal for low and high density samples at the same time.

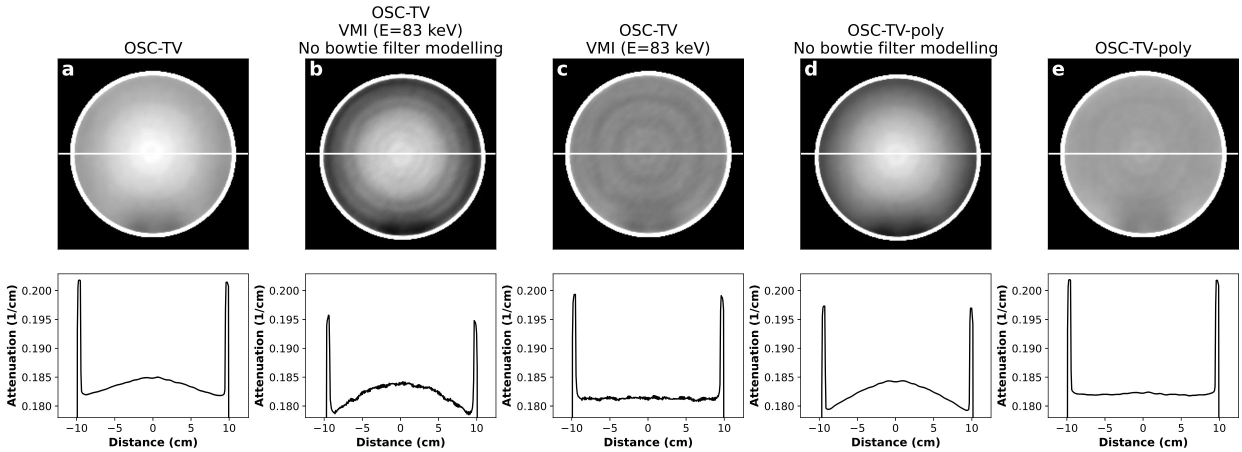

Figure 6: Water phantom: (a) reconstruction performed with OSC-TV (140 kVp), (b,c) virtual monoenergetic image calculated through DE-AM method (100/140 kVp), evaluated at 83 keV, without and with bowtie filter consideration, (d,e) reconstruction performed with OSC-TV-poly (140 kVp), without and with bowtie filter modelling. Window: [0.177,0.185] cm^{-1}.

3.3. Real samples application

The importance of the bowtie filter modelling for X-ray spectrum considerations in both BHC methods is shown in Fig. 6. Due to the presence of the bowtie filter in the CT scanner, an important *capping* artifact is produced in the water phantom (recalling that raw data were generated without manufacturer-provided BHC). The modelling of the bowtie filter, which provides a detector dependent spectra in the DE-AM and the polychromatic algorithms, significantly reduced this effect.

The effect of the regularization on the reconstruction of the photoelectric image is demonstrated in Fig.7. When no regularization is used in the reconstruction, hence the OSC algorithm, the resulted image is very noisy, presenting some peak values over the image. Although the mean pixel values are similar: 3873 for the OSC and 3825 for the OSC-TV, the first present a standard deviation of 1877, while the regularization is capable of reducing it to 197.

Figs. 8 and 9 show line profiles of the aluminum sample and the 50 % NaI solution without any BHC (a), the VMI for $E = 83\ keV$, which is a linear combination of the photoelectric and the Compton images, both reconstructed with OSC-TV (b), and finally, the reconstruction with the BHC from the proposed model (c). For higher density, higher Z samples, an important cupping

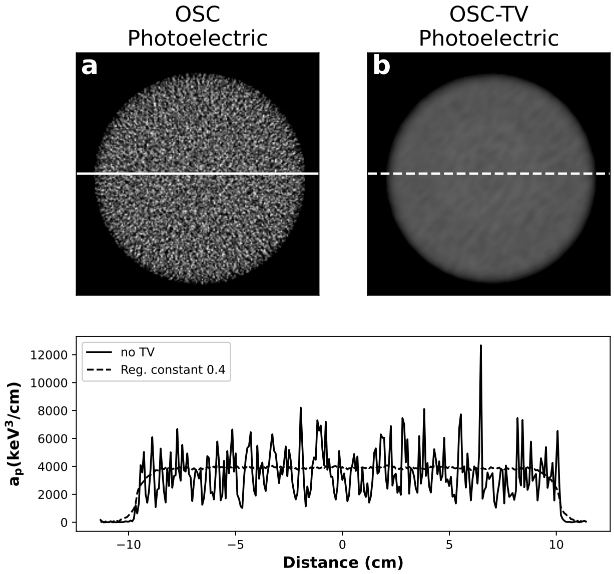

Figure 7: Water phantom: (a) reconstruction of the photoelectric image performed with OSC (no TV), (b) reconstruction of the photoelectric image performed with OSC-TV, with a regularization constant of 0.4. Window: [2,000,7,500] $keV^3\ cm^{-1}$.

artifact is observed in the uncorrected image of the aluminum sample and the 50 % NaI solution. Both BHC methods were able to reduce it.

Along the solid lines in shown in Fig. 6, one can see that the maximum and minimum value for the water phantom, when no BHC is applied (a), is 0.185 cm^{-1} and 0.182 cm^{-1}, respectively. The correspondent BHR is only 1.6 %. For the cases where BHC was attempted but with no filter considerations (b,d), the BHR increased to roughly 2.8%, where an overcorrection was produced. Finally, with the bowtie filter modelling, both BHC methods reduced the BHR to only 0.3 %, meaning the capping artifact was greatly reduced.

Concentric ring artifacts appears in the water phantom in Fig. 6 for all the cases studied, but mainly on the VMI image. These artifacts are the result of TV regularization, and so they can be reduced or removed by decreasing the regularization constant, at the expense of images reconstructed with more noise. The magnitude of these artifacts is increased by the window level/window width used, which is the same for all figures.

For the aluminum sample, the variations are more important, going from 0.52 cm^{-1} to 0.58 cm^{-1}

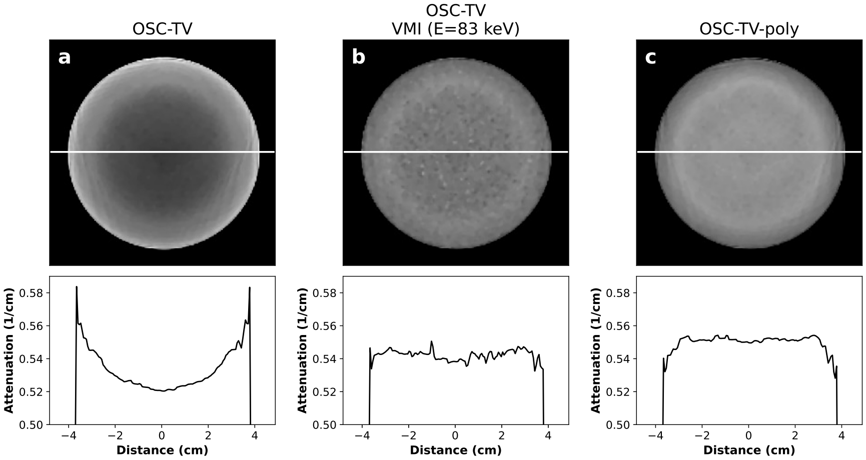

Figure 8: Aluminum sample: (a) reconstruction performed with OSC-TV (140 kVp), (b) virtual monoenergetic image calculated through DE-AM method (100/140 kVp), evaluated at 83 keV, (c) reconstruction performed with OSC-TV-poly (140 kVp). Window: [0.50,0.59] cm^{-1}.

in the image with no BHC, which represents a BHR of 10.3 %. The dual-energy and the OSC-TV-poly methods led to variations ranging from 0.53 cm^{-1} to 0.55 cm^{-1}, equivalent to a BHR of 3.6 %.

The OSC-TV-poly approach was able to reduce the cupping artifact importantly for the NaI solution (BHR of 3.6 %), even if the sample has an effective atomic number higher than the ones used to define the calibration curve, and a K-edge at 33.2 keV leading to a poor fit through Eq. 6 ($R^2 = 0.45$). This result is much better than the $BHR = 14.9$ % obtained without correction, and also lower than the dual-energy approach ($BHR = 5.9$ %). This last method led to an over-correction, as it can be seen in Fig. 9 (b), where a capping artifact is produced. The presence of a K-edge is poorly compatible with the two basis functions of the Alvarez and Macovski attenuation model (see Eq. 6), leading to this type of behavior [7, 8].

The proposed OSC-TV-poly method tends to produce smoother images, as it avoids the path taken by the DE-AM approach involving the generation of a potentially very noisy photoelectric image associated with low Z materials [6]. Although a comprehensive assessment is not conducted here since it is a non-issue with samples, the OSC-TV-poly method is also advantageous from a dosimetric perspective as it requires a single acquisition (compared to two with the DE-AM

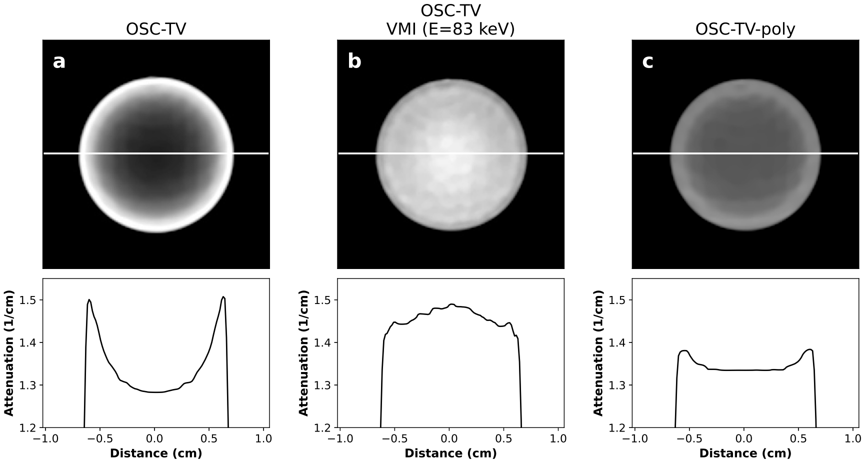

Figure 9: 50 % NaI solution: (a) reconstruction performed with OSC-TV (140 kVp), (b) virtual monoenergetic image calculated through DE-AM method (100/140 kVp), evaluated at 83 keV, (c) reconstruction performed with OSC-TV-poly (140 kVp). Window: [1.25,1.50] cm^{-1}.

method). A single acquisition is definitely an advantage in a clinical setting, where CT scans do not typically offer dual-energy capabilities (other than performing to separate acquisitions with the risk of misregistration of patient images).

Furthermore, the acquisition of high-Z and high density samples with reduced artifacts is also advantageous in the field of geology, such as porosity characterization in rocks with a CT scanner [31]. The presented algorithm can potentially deal with low and highly attenuation materials, such as water and dense rocks, improving the desired characterization by removing the bias caused by beam-hardening artifacts.

These results are important because they show that the calibration curve used, based on a large list of materials and NIST XCOM attenuation data, was able to estimate the photoelectric and Compton contribution for the materials in the virtual phantom, water phantom, the aluminum sample, and the 50 % NaI solution, which allowed beam-hardening to be simulated in the forward projection step, and ultimately, reconstruct images with reduced artifacts. Beam-hardening effects caused by the bowtie filter are also corrected by including its attenuation in the model. It is important to point out that all those samples presented an attenuation coefficient within the interval of validity of the calibration curve.

In this work, the X-ray spectrum provided by the manufacturer was not verified by independent means, hence, possible inaccuracies in such quantity could also lead to non-optimal beam-hardening correction [6, 8, 7] for both the methods presented in this work.

3.4. Pre-processing time

For the Siemens detector grid of 736 pixels x 64 pixels, and a total of 2,304 projections, the developed Python script, allied with the Numba compiler, is able to perform the dual-energy decomposition (Section 2.3) of such configuration in half a minute. That is, once the low- and high-voltage sinograms are acquired, it takes roughly 30 seconds to generate the Compton and photo-electric pair. For the 50 % NaI solution protocol, where twice the number of projections are used, the decomposition takes around 80 seconds.

3.5. Processing time

The OSC-TV-poly is computationally intensive. Hence, in order to evaluate the applicability of our method, we calculated the reconstruction time (min) of the ordinary OSC-TV against the OSC-TV-poly, using the 140 kVp images for benchmarking. As reported in Table 4, OSC-TV-poly is able to reconstruct the same images in a few minutes. For the water phantom, the reconstruction takes roughly 20 times longer than the OSC-TV, where it takes 3.3 and 8.3 times longer for the aluminum sample and the virtual phantom, respectively. This difference is more important for the water phantom due to its larger size (200 mm), where the X-ray spectrum needs to be estimated for more voxels compared to the aluminum sample. The reconstruction time of the virtual phantom takes longer compared to the water phantom and the aluminum cylinder due to the high number of subsets used in the reconstruction, which increases the number of iterations within a full OSC step.

For the 50 % NaI solution, processing time is longer due to its reconstruction matrix size (four times larger): almost two hours for the OSC-TV-poly and roughly 7 minutes for the OSC-TV. Such issue with the reconstruction time could be easily solved by making use of strategies to reconstruct regions-of-interests (ROI) through iterative reconstruction algorithms [28], hence, a smaller grid size could be used to avoid including the whole FOV into the image matrix and at the same time

Table 4
Comparison of reconstruction time using 4x nVidia Tesla V100 16 GB.

Sample	Reconstruction time (min)		Time increase
	OSC-TV	OSC-TV-poly	factor
Virtual phantom	1.86	6.13	3.30
Water phantom	0.21	4.36	20.76
Aluminum	0.47	3.87	8.23
50 % NaI	6.97	113.99	16.35

set smaller voxels sizes.

4. Conclusion

In this paper, a novel, physics-rich algorithm to reduce beam hardening artifacts was presented. The modelling of the physics allows the correction of beam hardening artifacts (capping, cupping and streaks) with no prior knowledge of the material information. The code can be implemented in the forward projection of an IR algorithm. Reasonable processing times were achieved by using multiple GPUs. Both the dual-energy method and the IR algorithm with a polychromatic acquisition model were able to deliver satisfactory results. The proposed approach outperformed the DE-AM BHC method when it comes to high-Z elements.

Author statement

The authors are fully aware and agree to the author order and the contents of this manuscript. Philippe Després is the corresponding author.

Funding

This research was supported by the Sentinel North program of Université Laval, made possible by the Canada First Research Excellence Fund. This work was also supported by a grant from *Fonds de recherche du Québec - Nature et technologies* [2018-PR-206076].

Declaration of competing interest

Karl Stierstorfer is an employee of Siemens Healthcare GmbH, Forchheim, Germany. The other authors declare that they have no conflict of interest to disclose.

Acknowledgements

We would like to thank Philippe Letellier and Mathieu des Roches for help in scanning the samples, prof. Dr. Damien Pham Van Bang for the support provided during the conception of this work, and Jérôme Landry and Pascal Bourgault for the essential help in setting the foundation of the algorithms used in this work. This research was made possible in part by support provided by WestGrid, Compute Canada and Calcul Québec. The operation of this supercomputer is funded by the Canada Foundation for Innovation (CFI), Ministère de l'Économie, des Sciences et de l'Innovation du Québec (MESI) and le Fonds de recherche du Québec – Nature et technologies (FRQ-NT).

CRediT authorship contribution statement

Leonardo Di Schiavi Trotta: Conceptualization, Methodology, Software, Data curation, Writing-Original draft preparation, Writing - Review & Editing, Visualization, Investigation, Formal analysis, Validation. **Dmitri Matenine:** Software, Writing - Review & Editing. **Margherita Martini:** Resources,Writing - Review & Editing. **Karl Stierstorfer:** Software,Writing - Review & Editing. **Yannick Lemaréchal:** Writing - Review & Editing. **Pierre Francus:** Conceptualization, Methodology, Investigation,Funding acquisition,Supervision,Writing - Review & Editing,Resources. **Philippe Després:** Conceptualization, Methodology, Investigation, Software,Funding acquisition,Project administration,Supervision,Writing - Review & Editing,Resources,Data Curation.

References

[1] G. v. Kaick, S. Delorme, Computed tomography in various fields outside medicine, Eur Radiol Suppl 15 (4) (2005) d74–d81. doi:10.1007/s10406-005-0138-1.
URL https://link.springer.com/article/10.1007/s10406-005-0138-1

[2] J. F. Barrett, N. Keat, Artifacts in CT: Recognition and Avoidance, Radiographics 24 (6) (2004) 1679–1691.
URL http://radiographics.rsna.org/content/24/6/1679.abstract

[3] B. D. Man, J. Nuyts, P. Dupont, G. Marchal, P. Suetens, An iterative maximum-likelihood polychromatic algorithm for CT, IEEE Transactions on Medical Imaging 20 (10) (2001) 999–1008. doi:10.1109/42.959297.

[4] L. Brabant, E. Pauwels, M. Dierick, D. Van Loo, M. A. Boone, L. Van Hoorebeke, A novel beam hardening correction method requiring no prior knowledge, incorporated in an iterative reconstruction algorithm, NDT & E International 51 (2012) 68–73. doi:10.1016/j.ndteint.2012.07.002.
URL http://www.sciencedirect.com/science/article/pii/S096386951200093X

[5] R. E. Alvarez, A. Macovski, Energy-selective reconstructions in X-ray computerized tomography, Phys Med Biol 21 (5) (1976) 733–744.

[6] Z. Ying, R. Naidu, C. R. Crawford, Dual energy computed tomography for explosive detection, Journal of X-Ray Science and Technology 14 (2006) 235–256.

[7] S. G. Azevedo, H. E. Martz, M. B. Aufderheide, W. D. Brown, K. M. Champley, J. S. Kallman, G. P. Roberson, D. Schneberk, I. M. Seetho, J. A. Smith, System-Independent Characterization of Materials Using Dual-Energy Computed Tomography, IEEE Transactions on Nuclear Science 63 (1) (2016) 341–350. doi:10.1109/TNS.2016.2514364.

[8] M. Paziresh, A. M. Kingston, S. J. Latham, W. K. Fullagar, G. M. Myers, Tomography of atomic number and density of materials using dual-energy imaging and the Alvarez and Macovski attenuation model, Journal of Applied Physics 119 (21) (2016) 214901. doi:10.1063/1.4950807.
URL https://aip.scitation.org/doi/abs/10.1063/1.4950807

[9] D. Fortin, P. Francus, A. C. Gebhardt, A. Hahn, P. Kliem, A. Lisé-Pronovost, R. Roychowdhury, J. Labrie, G. St-Onge, Destructive and non-destructive density determination: method comparison and evaluation from the Laguna Potrok Aike sedimentary record, Quaternary Science Reviews 71 (2013) 147 – 153. doi:https://doi.org/10.1016/j.quascirev.2012.08.024.
URL http://www.sciencedirect.com/science/article/pii/S0277379112003460

[10] L. A. Feldkamp, L. C. Davis, J. W. Kress, Practical cone-beam algorithm, Journal of the Optical Society of America A 1 (6) (1984) 612. doi:10.1364/JOSAA.1.000612.
URL https://www.osapublishing.org/abstract.cfm?URI=josaa-1-6-612

[11] D. Matenine, S. Hissoiny, P. Després, Gpu-accelerated few-view ct reconstruction using the osc and tv techniques, in: Proceedings of the 11th International Meeting on Fully Three-Dimensional Image Reconstruction in Radiology and Nuclear Medicine, 2011, potsdam, Germany.

[12] P. Després, X. Jia, A review of GPU-based medical image reconstruction, Phys Med 42 (2017) 76–92. doi:10.1016/j.ejmp.2017.07.024.

[13] Y. Zhao, M. Li, Iterative Beam Hardening Correction for Multi-Material Objects, PLOS ONE 10 (12) (2015) e0144607. doi:10.1371/journal.pone.0144607.
URL https://journals.plos.org/plosone/article?id=10.1371/journal.pone.0144607

[14] M. Krumm, S. Kasperl, M. Franz, Reducing non-linear artifacts of multi-material objects in industrial 3d computed tomography, NDT & E International 41 (4) (2008) 242–251. doi:10.1016/j.ndteint.2007.12.001.
URL http://www.sciencedirect.com/science/article/pii/S0963869507001478

[15] D. Matenine, Y. Goussard, P. Després, Evaluation of the OSC-TV Reconstruction Algorithm for Optical Cone-Beam Computed Tomography, in: D. Jaffray (Ed.), Proceedings of the IUPESM 2015 World Congress on Medical Physics and Biomedical Engineering, Vol. 51 of IFMBE Proceedings, Springer International Publishing, 2015, pp. 236–239.
URL http://dx.doi.org/10.1007/978-3-319-19387-8_57

[16] M. Slaney, A. Kak, Principles of computerized tomographic imaging, Society of Industrial and Applied Mathematics, 2001.
URL http://www.slaney.org/pct

[17] E. C. McCullough, Photon attenuation in computed tomography, Medical Physics 2 (6) (1975) 307–320. doi:10.1118/1.594199.

[18] R. A. Rutherford, B. R. Pullan, I. Isherwood, Measurement of effective atomic number and electron density using an EMI scanner, Neuroradiology 11 (1) (1976) 15–21. doi:10.1007/BF00327253.
URL https://link.springer.com/article/10.1007/BF00327253

[19] D. Matenine, Y. Goussard, P. Després, GPU-accelerated regularized iterative reconstruction for few-view cone beam CT, Med Phys 42 (4) (2015) 1505–1517. doi:10.1118/1.4914143.

[20] F. J. Beekman, C. Kamphuis, Ordered subset reconstruction for x-ray CT, Physics in medicine and biology 46 (7) (2001) 1835–1844.
URL http://stacks.iop.org/0031-9155/46/1835

[21] E. Y. Sidky, C.-M. Kao, X. Pan, Accurate image reconstruction from few-views and limited-angle data in divergent-beam CT, X-ray Sci. Tech. 14 (2) (2006) 119–139.
URL http://iospress.metapress.com/content/1jduv1cll3f9e2br/

[22] R. L. Siddon, Fast calculation of the exact radiological path for a three-dimensional CT array, Medical Physics 12 (2) (1985) 252–255.
URL http://link.aip.org/link/?MPH/12/252/1

[23] S. K. Lam, A. Pitrou, S. Seibert, Numba: A llvm-based python jit compiler, in: Proceedings of the Second Workshop on the LLVM Compiler Infrastructure in HPC, 2015, pp. 1–6.

[24] J. T. Bushberg, J. Bert, E. M. Leidholdt Jr., J. M. Boone, The essential physics of medical imaging, 3rd edition, Lippincott Williams and Wilkins, 2012.

[25] R. C. Murty, Effective Atomic Numbers of Heterogeneous Materials, Nature 207 (4995) (1965) 398. doi:10.1038/207398a0.
URL https://www.nature.com/articles/207398a0

[26] G. Landry, J. Seco, M. Gaudreault, F. Verhaegen, Deriving effective atomic numbers from DECT based on a parameterization of the ratio of high and low linear attenuation coefficients, Phys Med Biol 58 (19) (2013) 6851–6866. doi:10.1088/0031-9155/58/19/6851.

[27] A. E. Bourque, J.-F. Carrier, H. Bouchard, A stoichiometric calibration method for dual energy computed tomography, Physics in Medicine and Biology 59 (8) (2014) 2059–2088. doi:10.1088/0031-9155/59/8/2059.

[28] A. Ziegler, T. Nielsen, M. Grass, Iterative reconstruction of a region of interest for transmission tomography, Medical Physics 35 (4) (2008) 1317–1327. doi:10.1118/1.2870219.

[29] C. Suplee, XCOM: Photon Cross Sections Database (Sep. 2009).
URL https://www.nist.gov/pml/xcom-photon-cross-sections-database

[30] D. Barthelmy, Mineralogy database, accessed on 2021-04-20.
URL http://webmineral.com/

[31] S. Larmagnat, M. Des Roches, L.-F. Daigle, P. Francus, D. Lavoie, J. Raymond, M. Malo, A. Aubiès-Trouilh, Continuous porosity characterization: Metric-scale intervals in heterogeneous sedimentary rocks using medical CT-scanner, Marine and Petroleum Geology 109 (2019) 361–380. doi:10.1016/j.marpetgeo.2019.04.039.
URL https://www.sciencedirect.com/science/article/pii/S0264817219301898